

This is an Open Access document downloaded from ORCA, Cardiff University's institutional repository: <https://orca.cardiff.ac.uk/id/eprint/119811/>

This is the author's version of a work that was submitted to / accepted for publication.

Citation for final published version:

Michas, Marios, Ugalde Loo, Carlos , Ming, Wenlong , Jenkins, Nicholas and Runge, Stefan 2019. Maximum power extraction from a hydrokinetic energy conversion system. IET Renewable Power Generation 13 (9) , pp. 1411-1419. 10.1049/iet-rpg.2018.5642

Publishers page: <https://doi.org/10.1049/iet-rpg.2018.5642>

Please note:

Changes made as a result of publishing processes such as copy-editing, formatting and page numbers may not be reflected in this version. For the definitive version of this publication, please refer to the published source. You are advised to consult the publisher's version if you wish to cite this paper.

This version is being made available in accordance with publisher policies. See <http://orca.cf.ac.uk/policies.html> for usage policies. Copyright and moral rights for publications made available in ORCA are retained by the copyright holders.



# Maximum Power Extraction from a Hydrokinetic Energy Conversion System

Marios Michas<sup>1</sup>, Carlos E. Ugalde-Loo<sup>1\*</sup>, Wenlong Ming<sup>1</sup>, Nick Jenkins<sup>1</sup>, Stefan Runge<sup>1</sup>

<sup>1</sup> School of Engineering, Cardiff University, Queen's Buildings, The Parade, CF24 3AA, Cardiff, Wales, U.K.

\*[Ugalde-LooC@cardiff.ac.uk](mailto:Ugalde-LooC@cardiff.ac.uk)

**Abstract:** Hydrokinetic energy conversion systems capture the power available in the water flowing in waterways. An electrical interface for the power take-off of a hydrokinetic energy conversion system was designed and a control strategy for the maximum power extraction was investigated. A laboratory prototype was used for the experimental characterisation of the system. High efficiencies were observed due to the restricted flow conditions. The power curves obtained from the experimental results were used for the simulation of the system in MATLAB/Simulink. A 'perturb and observe' method was used for the maximum power point tracking. A control scheme based on a heuristic algorithm suitable for restricted and turbulent water flows was developed. A practical advantage of this scheme is that it does not require the use of mechanical sensors. The maximum power point tracking of the laboratory prototype was simulated and experimental validation undertaken, with simulation and experimental results agreeing well. The maximum power point tracking of a full-scale hydrokinetic energy conversion system was simulated to assess its performance towards practical deployment.

## 1. Introduction

Hydrokinetic energy conversion systems harvest the energy that is available in tidal currents, river streams and man-made waterways [1]. As there are thousands of miles of waterways around the world, this could potentially be a suitable renewable energy technology to extend the current hydroelectric capacity.

As in the case of variable-speed wind turbines, power electronics are used for the control of hydrokinetic energy conversion systems. The two basic configurations considered in the literature use either an active bridge rectifier or a diode-bridge rectifier and a dc-dc converter, followed by a three-phase inverter for the connection to the grid. Variable-speed operation below the rated water speed allows tracking of the maximum power point of the turbine [2], [3]. As a result, the efficiency of the system is maximised and the payback period of the installation costs reduced.

Since turbine-based hydrokinetic energy conversion systems are fairly new, their maximum power point tracking (MPPT) methods are often similar to those used in wind turbines [4]. The MPPT methods reported in the literature are either based on a predefined trajectory obtained from the turbine characteristics or on an iterative search. MPPT methods based on a predefined trajectory are widely used in large, grid-connected wind turbines [5], [6] and have been also discussed for tidal turbines [7]. However, 'perturb and observe' (heuristic) algorithms are often considered for standalone [8] and grid-connected small-scale turbines [9].

The principle of a 'perturb and observe' MPPT method is the perturbation of a control variable and the observation of the resulting electrical power. In [10] and [11], the MPPT of a wind turbine is achieved through the perturbation of the duty cycle of a dc-dc converter, while in [12] and [13], the perturbation is done through the rectifier voltage for the control of a standalone wind turbine. An optimal power curve combined with a heuristic algorithm is considered in [14] for the maximum power extraction from a

wind turbine. However, this control scheme is dependent on the turbine parameters. An adaptive MPPT algorithm for faster convergence for a wind energy conversion system is reported in [15]. The MPPT of wind turbines using fuzzy logic for the control of the firing angle of the inverter has been discussed in [16], while in [17] it was employed to estimate and compensate for the non-linearities and uncertainties in a wind energy conversion system. However, in these cases the complexity of the control scheme increases significantly. In [3], the MPPT of a river-current turbine is achieved through the perturbation of the rotational speed of the turbine. This MPPT method is based on knowledge transferred from the wind industry.

There have been significant research efforts reported in the open literature specifically directed to the MPPT of hydrokinetic turbines. For instance, an MPPT approach based on the regulation of the dc current for a predefined behaviour in the frequency of the electrical machine (PMSG) is proposed in [18]. A predefined trajectory is also used in [19] for the control of the torque of the hydrokinetic turbine along with a current meter. A similar approach is followed in [20], where vector control is adopted based on the measurement of the rotational speed of a turbine. In this case, the hydrokinetic energy conversion system is used to capture energy during the ship lock process in a hydraulic canal. In [21], a power signal feedback technique based on an MPPT scheme implemented as a look-up table is used to extract the maximum power of the turbine for a PMSG-based hydrokinetic turbine. The control scheme proposed in [22] for torque control is based on the knowledge of a factor  $K$  (related to the turbine parameters) and the square of the rotational speed. More complex methods are based on a three-dimensional MPPT model [23] or on neural network-based control schemes for the estimation of the turbine discharge [24]. However, such an increase in complexity may not be attractive from an industrial standpoint towards practical deployment.

It is relevant to mention that references [18]-[24] exploit the knowledge behind MPPT algorithms reported for wind applications. However, when such an approach is adopted the performance of the algorithms needs to be further investigated under the presence of restricted and turbulent water flows. In addition, it should be noticed that knowledge of the parameters and characteristics of the turbine and the need for sensors to measure mechanical signals is required in the work reported in the previous references for an adequate performance of the algorithms.

In this paper, a control scheme for the MPPT of a hydrokinetic energy conversion system for a man-made waterway is investigated. The control scheme is based on a ‘perturb and observe’ algorithm. It is a simple controller based on the perturbation of the rectifier voltage and, thus, no mechanical signal is needed. This simplicity offers a major practical advantage, with the presented scheme being particularly useful for kinetic energy turbines that are often located in constrained and turbulent water flows. For completeness, a laboratory prototype was developed to obtain the experimental characteristics of the hydrokinetic energy conversion system and to demonstrate the MPPT method.

## 2. Configuration of the hydrokinetic energy conversion system

The hydrokinetic energy conversion system investigated in this work is shown in Fig. 1. It consists of two identical vertical-axis turbines driving a permanent magnet synchronous generator (PMSG) through a common shaft. The design of the turbines is similar to that of a Gorlov turbine [25]. The power conversion system consists of a diode-bridge rectifier, a dc-dc converter and a three-phase inverter for the connection to the grid. A voltage source converter (VSC) is used for the grid connection of the system and to keep the voltage  $V_b$  constant. With a fixed voltage  $V_b$ , the dc-dc converter is used to provide a variable voltage  $V_{dc}$  for the control of the generator. The anticipated full-scale hydrokinetic energy conversion system is rated at 10 kW.

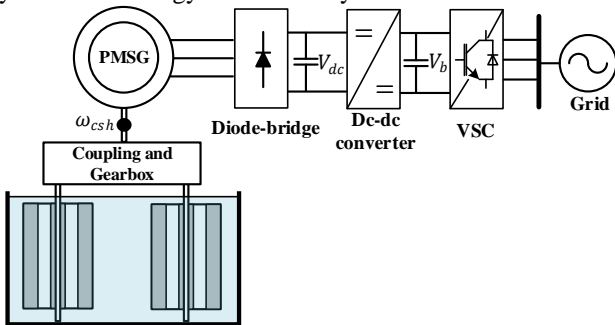


**Fig. 1.** Configuration of the hydrokinetic energy conversion system.

It should be highlighted that although a back-to-back configuration based on VSCs is the prominent alternative for power conversion systems, this was not adopted in this paper. The hydrokinetic energy conversion system studied in this work is intended for a low-rated canal application—which could be also adopted in standalone systems. Given that the employed MPPT algorithm is a practical solution that does not require sensors for mechanical signals or prior knowledge of the turbine characteristics, this was complemented with the adoption of a diode-bridge rectifier. This is a simple, robust and economic alternative that eliminates the need for a VSC

rectifier terminal. For its implementation, the dc-dc converter is used to control the rectifier voltage as this may facilitate the connection of a battery energy storage system. The VSC inverter terminal is employed for grid integration.

## 3. Modelling of the system

### 3.1. Hydrodynamic model

The hydrodynamic model shown in Fig. 2 is used to calculate the torque produced by the turbines. The speed of the common generator shaft,  $\omega_{csh}$ , is measured and the rotational speed of each turbine,  $\omega_t$ , is calculated using the gearing ratio,  $N$ . This way, the tip-speed ratio,  $\lambda$ , is obtained and a look-up table is used to determine the power coefficient,  $C_p$ . Although there is mechanical coupling between the two turbines, it was assumed that there is no hydrodynamic interaction between each other. Thus, the power available in the water is calculated using:

$$P_{fl} = \frac{1}{2} \cdot \rho \cdot 2A \cdot v_{fl}^3, \quad (1)$$

where  $\rho$  is the water density (997 kg/m<sup>3</sup>),  $A$  is the swept area of each turbine, and  $v_{fl}$  is the water speed.

The power captured by the turbines is calculated using the power coefficient and divided by the rotational speed of the common shaft so that the mechanical torque of the common shaft,  $\tau_{hyd}$ , is obtained.

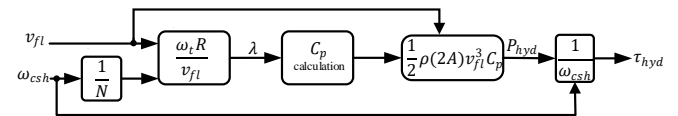


**Fig. 2.** Hydrodynamic model.

### 3.2. Drive-train Model

A single-mass (lumped) representation was used to model the drive-train of the system. This is described by

$$\frac{d\omega_{csh}}{dt} = \frac{T_{hyd} - T_{em}}{J_{total}}, \quad (2)$$

where  $J_{total}$  is the total inertia of the rotating mass and  $T_{em}$  is the electromagnetic torque of the generator. The total inertia of the system is given by

$$J_{total} = J_{2t} + J_{gen}, \quad (3)$$

where  $J_{2t}$  is the total inertia of the two turbines and  $J_{gen}$  is the inertia of the generator. Details of the calculation of the total inertia of the system are given in the Appendix.

It could be argued that the single-mass drive-train model given by equations (2) and (3) is arguably simple as it does not consider the mechanical coupling between the two turbines of the hydrokinetic energy conversion system. However, this model is sufficient to reproduce the phenomena of interest despite its simplicity, as shown by the simulation and experimental results reported in Section 6. The mathematical derivation of a more detailed drive-train model and/or the use of two-mass or three-mass models where bending dynamics and frequency of oscillations can be represented more faithfully [26], [27] are out of the scope of this work.

### 3.3. Generator model

The PMSG model in a  $dq$  frame is given in [28] as

$$\frac{d}{dt} i_d = \frac{1}{L_d} u_d - \frac{R_s}{L_d} i_d + \frac{L_q}{L_d} n_{pp} \omega_{gen} i_q, \quad (4)$$

$$\frac{d}{dt} i_q = \frac{1}{L_q} u_q - \frac{R_s}{L_q} i_q - \frac{L_d}{L_q} n_{pp} \omega_{gen} i_d - \frac{\psi_m n_{pp} \omega_{gen}}{L_q}, \quad (5)$$

$$\tau_{em} = \frac{3}{2} p [\psi_m i_q + (L_d - L_q) i_d i_q], \quad (6)$$

where  $L_d, L_q$  (H) are the self-inductances of the stator;  $R_s$  ( $\Omega$ ) is the stator resistance;  $u_d, u_q$  (V) are the stator voltages;  $i_d, i_q$  (A) are the stator currents;  $\psi_m$  (V·s) is the flux linkage of the permanent magnet;  $p$  is the pole pairs; and  $\omega_{gen}$  is the generator mechanical speed.

A PMSGs is adopted in this work as it is preferred for variable-speed operation in renewable energy applications. Contrary to electrically excited synchronous machines, PMSGs do not require an external dc supply, slip rings and contact brushes [21]. With respect to induction machines, PMSGs operate at a higher power factor, have an increased power density large enough to offset the cost of permanent magnets, do not require reactive support and are suitable for multi-pole constructions with low rotor speeds where the use of a gearbox may be avoided [29]—such as in a hydrokinetic energy conversion system.

### 4. Experimental characterisation

A laboratory prototype was used to experimentally obtain the steady-state characteristic curves of the system. The laboratory prototype is rated at 200 W and, instead of a VSC, batteries were used to fix voltage  $V_b$  (see Fig. 3).

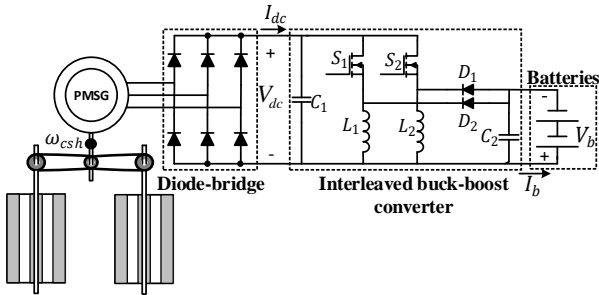


Fig. 3. Configuration of the laboratory prototype.

Two small-scale vertical-axis turbines were fixed on the bottom of an 18 m flume. A timing belt and three pulleys were used to transfer the rotation of the turbines into the rotation of a common shaft. Identical pulleys were put on the rotor of each turbine. The timing belt was used to connect these separate pulleys with the third pulley fixed on the common shaft. This way, synchronised counter-rotation of the turbines was ensured. The ratio between the radius of the pulleys of each turbine and the radius of the pulley of the common shaft defined the gearing ratio  $N$ .

The common shaft was used to drive a 200 W PMSG. The generator's output was connected to two 12 V batteries through a diode-bridge rectifier and an interleaved buck-boost converter. In the continuous conduction mode of the converter, the ratio between voltages  $V_{dc}$  and  $V_b$  is [30]

$$\frac{V_b}{V_{dc}} = \frac{D}{1 - D}, \quad (7)$$

where  $D$  is the duty cycle of the converter. The interleaved operation was achieved by operating the two switches of the converter with a phase difference of  $180^\circ$ . The switching frequency was set to 100 kHz.

According to (7),  $V_{dc}$  can either be higher or lower than  $V_b$  and, therefore, a wide area of operation was ensured. The uncontrolled rectifier, the dc-dc converter, and the capacitors were fixed in an enclosure for safety. A computer was used to control the buck-boost converter. The experimental set-up is shown in Fig. 4.

For the experimental procedure, the water level in the flume, the dimensions, and the distance between the shafts of the two identical turbines and the gearing ratio were set. This information is provided in Table 1. For the measurement of the mechanical torque and the rotational speed, a device combining a torque transducer and a speed encoder [31] was fixed on the common shaft. The frequency of the measurements was 100 Hz. An oscilloscope was used to measure voltages  $V_{dc}$  and  $V_b$  and currents  $I_{dc}$  and  $I_b$ .

The water speed was varied using a pump controlled remotely from a control panel. The flow speed was varied by regulating the electrical power applied to the impeller of the flume. Following a similar procedure as the one reported in [32], the flow speeds were analysed at certain water depths and pump powers using an acoustic Doppler velocimeter (ADV). It was found that when the pump operates at 25% of its capacity and for a water height of 0.5 m, a bulk flow velocity of 0.72 m/s occurs. Values of 0.85 m/s at 30%, 0.98 m/s at 35% and 1.09 m/s at 40% were obtained also for a water height of 0.5 m. The bulk velocities are the averaged values of several ADV point readings across the cross-section of the flume. These water speeds were used for the experiment.

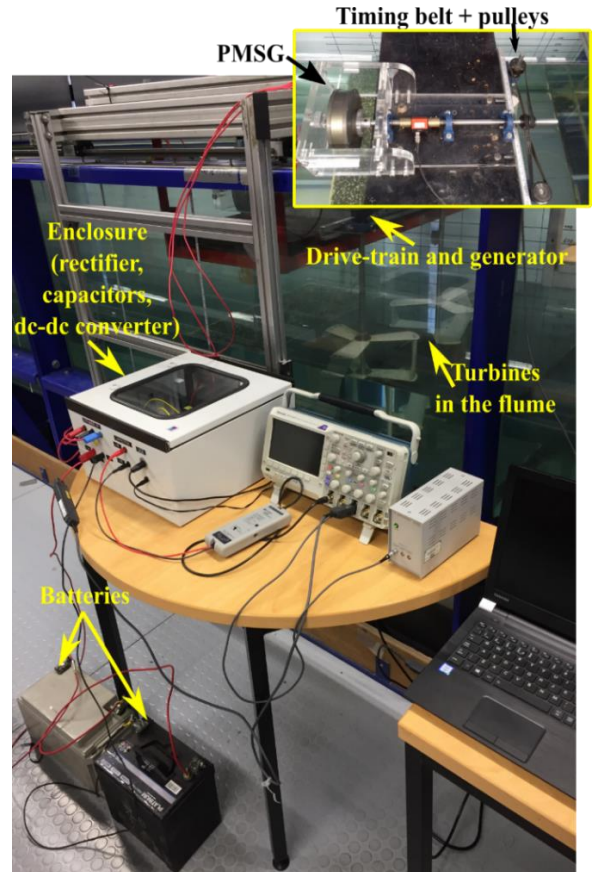


Fig. 4. Experimental set-up.

**Table 1.** Specifications for the laboratory prototype and the full-scale system

| Variable                                  | Experimental prototype | Prototype simulation | Full-scale system simulation            |
|---|------------------------|----------------------|---|
| $T_s$ (s)                                 | 0.5 s                  | 0.5 s                | 1 s                                     |
| $S$ (V)                                   | 0.2 V                  | 0.2 V                | 5 V                                     |
| $K_p$                                     | 0.01                   | 0.2                  | 1                                       |
| $K_i$                                     | 100                    | 400                  | 100                                     |
| $T_c$ (s)                                 | 0.45 s                 | –                    | –                                       |
| DC-dc converter switching frequency (kHz) | 100                    | 100                  | 100                                     |
| Estimated inertia (kg·m <sup>2</sup> )    | –                      | 0.0876               | 9.43                                    |
| $V_{dc}/k_{rpm}$                          | 190                    | 190                  | 3460                                    |
| Number of poles                           | 16                     | 16                   | 24                                      |
| Rated power of PMSG (kW)                  | 0.2                    | 0.2                  | 10                                      |
| Rated speed of PMSG (rpm)                 | 200                    | 200                  | 200                                     |
| $R_{L-L}@20^\circ\text{C}$ ( $\Omega$ )   | 0.8                    | 0.8                  | 3.53                                    |
| $L_{L-L}@20^\circ\text{C}$ (mH)           | 7.4                    | 7.4                  | 78.2                                    |
| Batteries (V)                             | 12                     | 12                   | –                                       |
| Grid                                      | –                      | –                    | $V_{L-L,rms} = 200$ V,<br>$f_g = 50$ Hz |
| Turbine dimensions                        | 0.3x0.18 m             | 0.3x0.18 m           | 0.8x1.36 m                              |
| Gearing ratio                             | 4:3                    | 4:3                  | 3:1                                     |
| Volume of the blade (mm <sup>3</sup> )    | 271064.5               | 271064.5             | 3391389                                 |
| Density of the blade (g/cm <sup>3</sup> ) | 0.93                   | 0.93                 | 2.7                                     |
| Mass of the blade (kg)                    | 0.287                  | 0.287                | 17.3                                    |

**Note:** the proportional and integral gains of the PI controllers were chosen following a heuristic method aiming to achieve a transient response with a limited overshoot for reference step changes for voltage  $V_{dc}$ . It should be noted that although the inertia of the full-scale system and the voltage constant of the PMSG are higher than for the laboratory prototype, the rated speed of the PMSG for all configurations is the same. Therefore, an independent scaling-up of the turbines and of the PMSG was made independently. As a result, the gains of the controller had to be reselected for the simulation of the full-scale system.

For every water speed, the buck-boost converter was controlled using a proportional-integral (PI) control structure to decrease  $V_{dc}$  from the no-load value down to zero. The gains of the PI controller are given in Table 1. Step changes of 1 V were applied every 10 s. A low-pass filter with a time constant of 1 s was used for the offline filtering of the measurements.

The mechanical power  $P_m$  was calculated using the torque and the speed measurements of the common shaft. The power flowing into the batteries  $P_b$  was calculated using the measurements of voltage  $V_b$  and current  $I_b$ .

The power coefficient  $C_p$  of the system was calculated using

$$C_p = \frac{P_m}{P_{fl}}. \quad (8)$$

The tip-speed ratio for this system was calculated, referring to one of the two turbines, using

$$\lambda = \frac{\omega_t R}{v_{fl}}, \quad (9)$$

where  $\omega_t$  is the rotational speed of each turbine obtained from the speed of the common shaft using the gearing ratio  $N$ .

Fig. 5(a) shows the steady-state characteristic ( $C_p - \lambda$ ) curve of the system. Although a unique curve was expected regardless of water speed, different curves were obtained instead due to losses in the test system. Fig. 5(b) shows the power flowing into the batteries versus the rotational speed of the common shaft for different water speeds. For very low voltages (1–4 V) and thus rotational speeds, the system was unstable and no accurate measurements could be taken. Consequently, the  $C_p - \lambda$  curves of Fig. 5(a) were neither obtained for very low tip-speed ratios nor the power curves shown in Fig. 5(b) for very low rotational speeds of the common shaft.

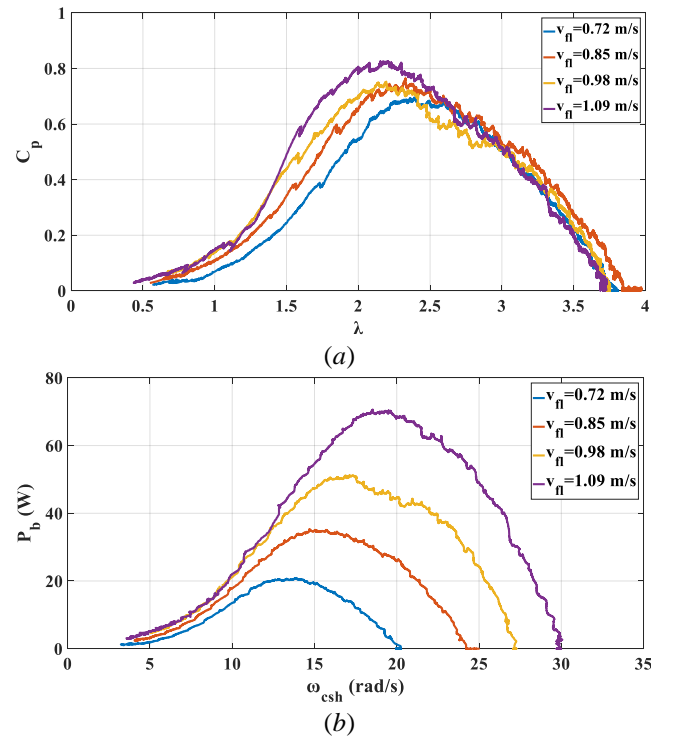


**Fig. 5.** Characteristic curves of the hydrokinetic energy conversion system. (a) Steady-state  $C_p - \lambda$  curves. (b) Power flowing into the batteries versus rotational speed of the common shaft.

As shown in Fig. 5(a), the power coefficient for all curves exceeds the Betz limit (0.593) [33]. This is because the Betz limit applies for turbines operating under unconstrained flow conditions. However, for the hydrokinetic energy conversion system tested in this work, restricted flow conditions were adopted. Blockage provided by the flume was used to represent the blockage effect that might be expected in real conditions. It should be highlighted that the system of identical turbines investigated in this work is intended for a canal application, which is an enclosed, constrained and blocked environment. In such conditions, the definition of the power coefficient may not be within the same boundaries for which the Betz limit is defined as the walls of the flume (and thus of the canal in a full-scale application) would act as an augmentation mechanism increasing the efficiency of the system [34].

## 5. Maximum power extraction

### 5.1. Analysis of the 'perturb and observe' method

As shown in Fig. 5(b), for a specific water speed, at the maximum power point,

$$\frac{dP}{d\omega_{csh}} = 0. \quad (10)$$

For vertical-axis turbines with fixed pitch blades, the power coefficient  $C_p$  is a function of the tip-speed ratio  $\lambda$ . Therefore, the power captured by the two turbines of the hydrokinetic energy conversion system is given by

$$P = \frac{1}{2} \rho (2A) v_{fl}^3 C_p(\lambda). \quad (11)$$

The two turbines are synchronised and counter-rotate with the same rotational speed  $\omega_t$ . Given a gearing ratio  $N$ , the relationship between the rotational speed of each turbine and the rotational speed of the common shaft is given by

$$\omega_t = \frac{\omega_{csh}}{N}. \quad (12)$$

The common shaft drives the PMSG. Thus, the rotational speed of the common shaft  $\omega_{csh}$  is the same as the rotational speed of the generator. Therefore,  $\omega_{csh}$  is linked to the electrical angular frequency of the generated voltage  $\omega_e$  by

$$\omega_e = p \cdot \omega_{csh}. \quad (13)$$

In [35], it is shown that the rectified voltage  $V_{dc}$  is a function of the electrical angular frequency  $\omega_e$ :

$$V_{dc} = V_{dc}(\omega_e), \quad (14)$$

and

$$\frac{dV_{dc}}{d\omega_e} > 0. \quad (15)$$

From (11)–(14), considering (9), it is deduced that

$$P = P(V_{dc}(\omega_e(\omega_{csh}))). \quad (16)$$

Therefore, applying the differentiation chain rule to composite function (16) while considering (11), (13) and (14), condition (10) is written as follows

$$\frac{dP}{d\omega_{csh}} = \frac{dP}{dV_{dc}} \cdot \frac{dV_{dc}}{d\omega_e} \cdot \frac{d\omega_e}{d\omega_{csh}} = 0. \quad (17)$$

From (13), it is concluded that

$$\frac{d\omega_e}{d\omega_{csh}} = p > 0. \quad (18)$$

Thus, from (10), considering (15) and (18), at the maximum power point,

$$\frac{dP}{dV_{dc}} = 0. \quad (19)$$

The following expression is used as the basis of the 'perturb and observe' algorithm [3]:

$$V_{dc,k} = V_{dc,k-1} + \int_{\tau=t_{k-1}}^{\tau=t_k} S \cdot \text{sgn}(P_k - P_{k-1}) \cdot \text{sgn}(V_{dc,k} - V_{dc,k-1}) d\tau \quad (20)$$

A sampling period  $T_s$  is used, where index  $k$  in (20) denotes successive discrete time points such that  $T_s = t_k - t_{k-1}$ .  $V_{dc,k}$  and  $P_k$  are the values of the rectifier voltage and the power at time  $t_k$  and  $S$  is the convergence speed coefficient.

According to (20), the voltage  $V_{dc}$  is perturbed and the resulting power  $P$  is measured. For a specific perturbation of  $V_{dc}$ , if the electrical power is increased, then a step change  $S$  in voltage with the same sign takes place. Otherwise, if power is decreased, the same step change takes place but with a reversed sign. If there is no change in the power,  $V_{dc}$  remains constant.

### 5.2. Control scheme for maximum power extraction

Fig. 6 shows the control scheme for the MPPT of the laboratory prototype. For a constant voltage  $V_b$  fixed by the batteries, the dc-dc converter is used for the control of voltage  $V_{dc}$  for the MPPT.

The voltage  $V_{dc}$  and the current  $I_{dc}$  are measured every 10  $\mu$ s. In the laboratory prototype three-bladed vertical-axis turbines are employed, which exhibit characteristic 3P oscillations (i.e. oscillations in torque and speed with a frequency of three-times the rotational speed) [36]. To eliminate the effect of the 3P oscillations in the MPPT algorithm, a low-pass filtering with a time constant  $T_c$  is used. Then, the generated power  $P$  is calculated and used as an input to the MPPT stage. At the MPPT stage, a reference value for the voltage  $V_{dc}^*$  is chosen according to (20). The difference between the measured and the reference value of the voltage  $V_{dc}$  is fed to a PI controller. The PI controller generates the input signal for the pulse-width modulation (PWM) generator for the control of the dc-dc converter.

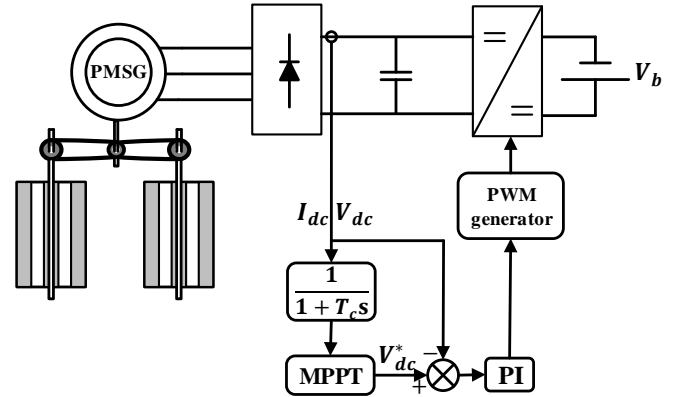


Fig. 6. Control scheme for the hydrokinetic energy conversion system.

To assess the performance of the MPPT algorithm, the convergence speed coefficient, the sampling time and the time constant of the low-pass filter were set and are given in Table 1 along with the parameters of the PMSG, the gains of the controller, and the dimensions of the turbines.

**Note:** It should be noticed that by varying (i.e. perturbing)  $V_{dc}$ , the terminal voltage of the PMSG is changed, which, in turn changes the rotational speed of the generator. Consequently, the torque changes and the resulting power can be measured (i.e. observed). This way, the maximum power point of the  $C_p - \lambda$  curve can be tracked. This approach makes the control scheme attractive for a practical application as it is simple and does not require sensors for mechanical signals. The presented 'perturb and observe' MPPT algorithm could be adopted in the real full-scale hydrokinetic energy conversion system as no extreme changes in the water speed would be expected.

## 6. Simulation and experimental results

### 6.1. MPPT of the laboratory-scale hydrokinetic energy conversion system: simulation and experimental validation

The laboratory prototype was simulated, prior to the experimental validation of the control scheme for the MPPT. For the simulation of the laboratory system, the batteries were represented by an ideal dc voltage source in series with a very small resistance. The power coefficient  $C_p$  was calculated with the aid of a look-up table which considered the data provided by the experimental results shown in Fig. 5(a). The gains of the controller were tuned and are given in Table 1.

The inertia of the laboratory-scale system was estimated and is given in Table 1. To validate this estimated value, a step change in voltage  $V_{dc}$  from 38 to 16 V was applied both in simulation and experimentally. Results are shown in Fig. 7. It is observed that there are oscillations present in the experimental results. This oscillatory behaviour, known as 3P oscillation (or ripple), is exhibited by practical vertical-axis turbines such as the one used in this work—as discussed in Section 5.2. However, the 3P oscillation was neglected in the simulation model and was thus not present in the simulation results. It is also shown that for the same change in dc voltage, the time needed for the rotational speed to settle to its new value is approximately the same for both the simulation and the experimental test rig. Consequently, the calculations provided a realistic approximation of the inertia of the laboratory prototype of the system.

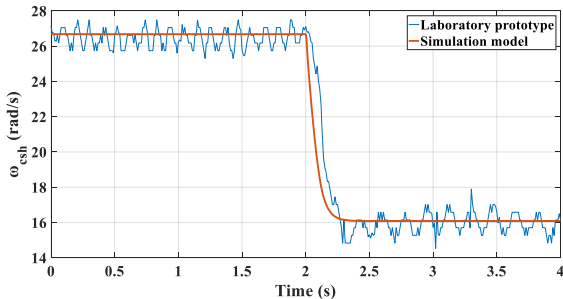


**Fig. 7.** Response of the rotational speed of the common shaft of the laboratory prototype (blue curve) and of the simulation model (red curve) for a step change in  $V_{dc}$  from 38 to 16 V.

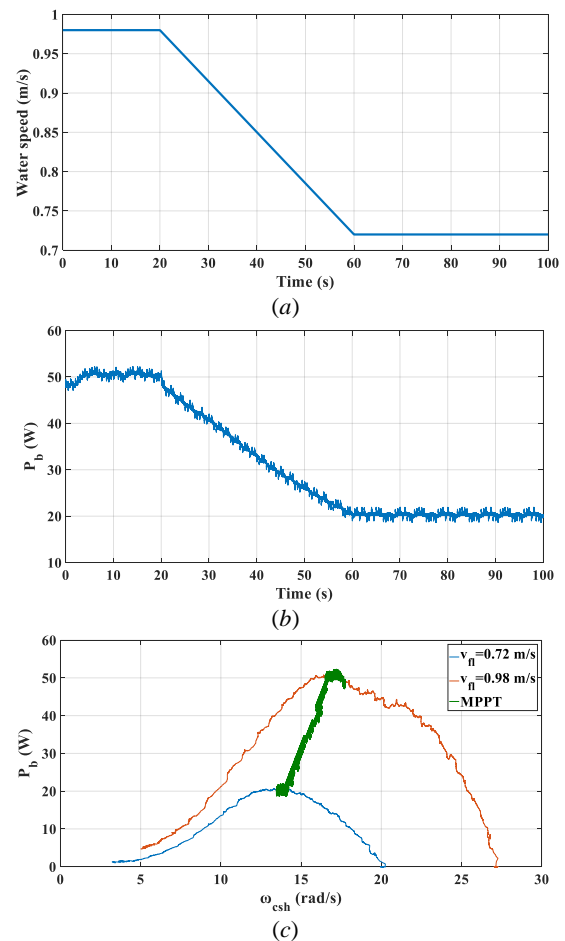
For the simulation of the laboratory prototype, the convergence speed coefficient  $S$  was selected to provide a change in the rotational speed of 0.1 rad/s. The sampling time  $T_s$  of the MPPT algorithm was selected based on the response of the rotational speed of the common shaft for a step change  $S$  in the voltage  $V_{dc}$ . Both  $S$  and  $T_s$  are given in Table 1. The 3P oscillations of the rotational speed and, thus, the voltage  $V_{dc}$ , were neglected. Therefore, no low-pass filtering was used in the simulation.

The water speed was linearly decreased from 0.98 to 0.72 m/s, with results shown in Fig. 8. Fig. 8(a) shows the change in the water speed. Fig. 8(b) shows the power flowing into the batteries. Fig. 8(c) shows the power flowing into the batteries against the rotational speed of the common shaft of the simulated laboratory-scale system. The blue curve is the power curve of the laboratory prototype for a water speed of 0.72 m/s and the red curve is for a water speed of 0.98 m/s. The green curve shows the simulation of the tracking procedure. Maximum power extraction was achieved for both

water speeds and the tracking of the maximum power point was maintained during the change in the water speed.

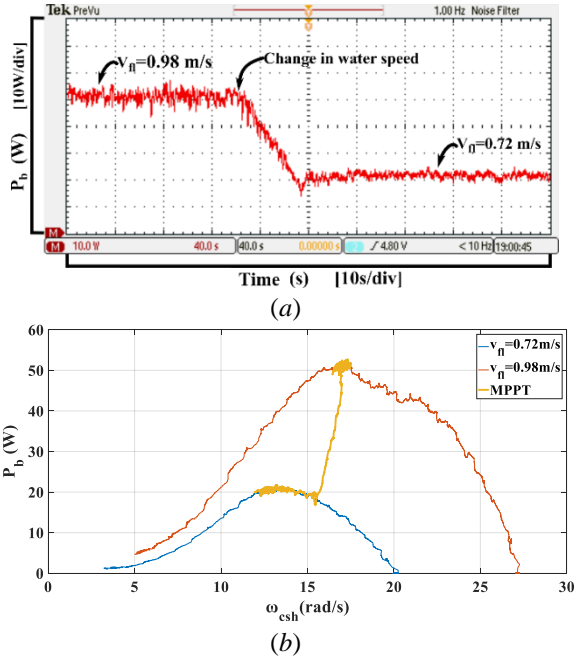
The sampling time and the convergence speed coefficient selected for the simulation of the MPPT of the laboratory-scale hydrokinetic energy conversion system were used for the experimental validation of the MPPT of the laboratory prototype. The results were filtered offline as described in Section 4.

For the experimental procedure, a change in the water speed of the flume was applied from 0.98 to 0.72 m/s similarly to the one shown in Fig. 8(a). Fig. 9(a) shows an oscilloscope screenshot of the power flowing into the batteries. The power was obtained by measuring the voltage across the terminals of the batteries and the current flowing into the batteries. It is shown that when the change in the water speed took place, the power decreased to a minimum point. Then, it settled and oscillated around a new value due to the new water flow condition.



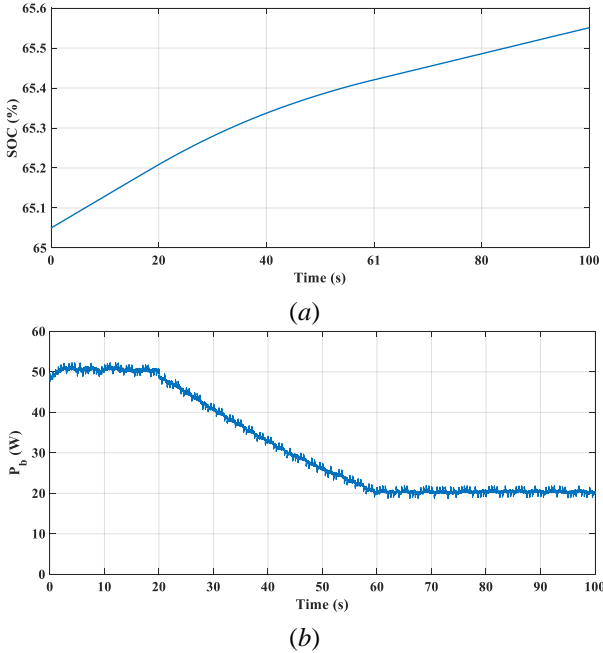
**Fig. 8.** Simulation of the laboratory prototype: (a) water speed, (b) power flowing into the batteries, (c) power flowing into the batteries vs. the rotational speed of the common shaft.

Fig. 9(b) shows the power flowing into the batteries against the rotational speed of the common shaft of the laboratory prototype. As it can be observed, the curves are similar to those in Fig. 8(c). The yellow curve shows the MPPT procedure of the laboratory test system. At first, for a water speed of 0.98 m/s, the system was operating around the maximum power point. When the water speed was decreased to 0.72 m/s, an overspeed occurred. Then the maximum power point for the new water speed condition was reached and an oscillation around the new maximum power point was observed.



**Fig. 9.** Experimental results: (a) oscilloscope screenshot of the power flowing into the batteries; (b) power flowing into the batteries vs. the rotational speed of the common shaft.

**Note:** it could be argued that the use of an ideal dc voltage source to represent the battery in the simulation studies may be an oversimplification given the availability of battery models in MATLAB/Simulink. To examine this in more detail, the simulation of the laboratory scale prototype was repeated with a battery model included, with results shown in Fig. 10. The state-of-charge of the battery is shown in Fig. 10(a) and the power flowing into the battery model shown in Fig. 10(b). As, it can be observed, the addition of the battery model does not represent a substantial difference in performance compared to when an ideal dc voltage source is employed (see Fig. 8(b)). Thus, no further discussion is warranted.



**Fig. 10.** Simulation of the laboratory prototype with a battery model: (a) state-of-charge of the battery; (b) power flowing into the battery.

## 6.2. Simulation of a full-scale hydrokinetic energy conversion system

The full-scale (10 kW) hydrokinetic energy conversion system was modelled and simulated to assess the performance of the MPPT control scheme for a larger system inertia and voltage constant of the generator. The sampling time of the Simulink file was set to be the same as in the case of the simulation of the laboratory prototype ( $10^{-5}$  s). An ideal ac voltage source and a phase reactor were used to represent the grid. For the VSC control, a phase-locked loop was used to measure the frequency of the grid, an inner loop for the control of the current in the  $dq$  frame, and an outer loop to control voltage  $V_b$  and fix it at 400 V. The control of the grid-side VSC is described in detail in [37]. Details on the turbine dimensions, the gearing ratio of the drive-train, the estimated inertia of the system, the generator and the grid of the full-scale system are given in Table 1.

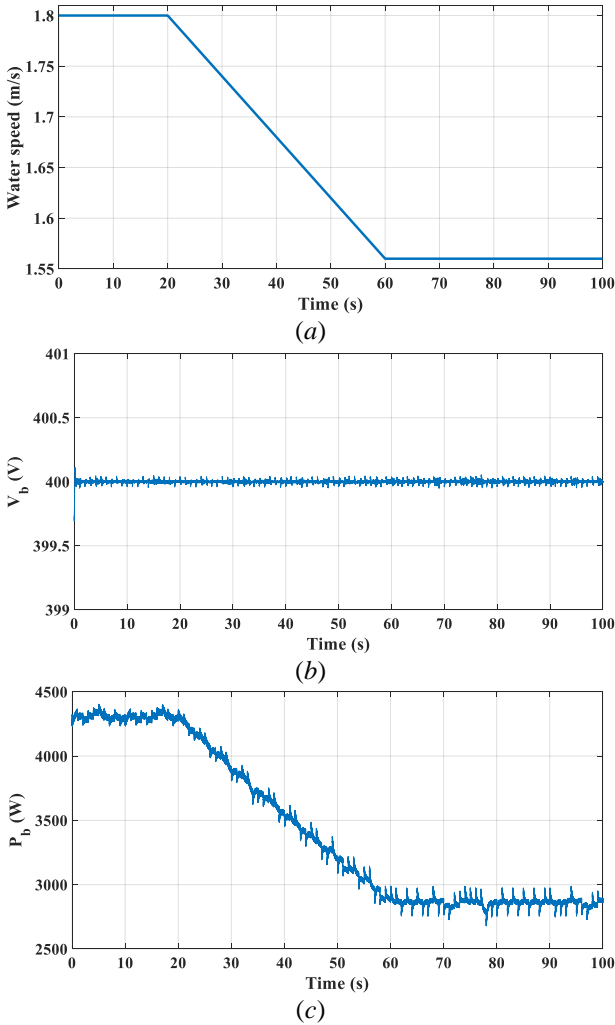
Due to lack of availability in the open literature of  $C_p - \lambda$  curves for a full-scale hydrokinetic energy conversion system for man-made waterways, data from the experimental characterisation of the laboratory prototype were used instead. In this specific case, the power coefficient  $C_p$  was calculated with the aid of a look-up table derived from the experimental results shown in Fig. 5(a) for a water speed of 0.98 m/s. It was assumed that this curve was the unique power curve for all the water speeds of the full-scale system.

Due to the higher inertia of the full-scale system, a higher sampling time  $T_s$  for the MPPT algorithm was selected compared to the one employed for the simulation of the laboratory prototype. Although the PMSG selected for the full-scale system is rated at 10 kW, its rated speed is the same as that of the PMSG in the laboratory (rated at 200 W). Therefore, the voltage constant of the PMSG of the full-scale system is higher than that of the laboratory prototype and, thus, a higher speed coefficient  $S$  was also selected. The values of both  $S$  and  $T_s$  are given in Table 1.

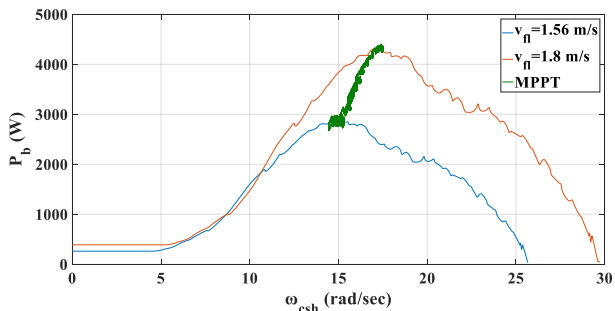
For the simulation of the maximum power extraction from the full-scale 10 kW system, a change in the water speed from 1.8 to 1.56 m/s was applied as this range of speeds is achieved on-site inside the canal. This is different from the range of speeds used for the laboratory prototype. In this case, a linear decrease was assumed as shown in Fig. 11(a). Voltage  $V_b$  was properly controlled and fixed at 400 V, as shown in Fig. 11(b). The resulting power flowing from the dc-dc converter to the VSC,  $P_b$ , is shown in Fig. 11(c).

Fig. 12 shows the power flowing from the dc-dc converter to the VSC against the rotational speed of the common shaft of the hydrokinetic energy conversion system. The blue curve is the power curve of the hydrokinetic energy conversion system for a water speed of 1.56 m/s. The red curve is the power curve for a water speed of 1.8 m/s. The green curve shows the simulation of the tracking procedure. As in the case of the laboratory-scale system, the maximum power extraction was achieved for both water speeds.

As it has been shown in the results reported in this section, a good performance of the ‘perturb and observe’ MPPT algorithm is exhibited both in computer simulations and experimental tests. This, together with its practical advantages, makes of the algorithm a potential alternative for small-scale vertical-axis wind turbine configurations under the presence of turbulent conditions—however, this requires further investigation which falls out of the scope of this paper.



**Fig. 11.** Simulation of the MPPT of the full scale hydrokinetic energy conversion system: (a) water speed, (b) voltage  $V_b$  and (c) power flowing from the dc-dc converter to the VSC.



**Fig. 12.** Power flowing from the dc-dc converter to the VSC against the rotational speed of the common shaft of the simulated full-scale hydrokinetic energy conversion system.

## 7. Conclusions

The use of hydrokinetic energy conversion systems in man-made waterways is a new concept and the maximum power extraction is of high interest. An advantage of the MPPT approach presented in this paper is its simplicity and suitability for low-rated canal applications. It provides a practical technique to deal with uncertainties in the turbine characteristics and MPPT can be achieved under restricted and turbulent water flows. In addition, no sensors for mechanical signals are required—thus reducing the complexity and cost of the system. This way, the control

scheme objective reduces to the control of the diode-bridge rectifier voltage using a dc-dc converter.

The work presented in this paper goes beyond computational simulation-based verification as a laboratory prototype was developed for the experimental validation of the ‘perturb and observe’ MPPT-based control scheme. The steady-state characteristic curves of the hydrokinetic energy conversion system indicate a high system efficiency due to the restricted water flow conditions. To mitigate the effect of 3P oscillations characteristic to the rotation of three-bladed vertical-axis turbines in the dc voltage, low-pass filtering of the rectifier voltage and current was used.

Simulation results indicated the dependence of the selection of sampling time of the MPPT algorithm on the inertia of the system. Additionally, the performance of the convergence speed coefficient was directly affected by the voltage constant of the generator used.

## 8. Acknowledgement

This work was supported in part by the EU FP7 Programme through the project “Beyond State of the art Technologies for repowering AC corridors & multi-Terminal HVDC Systems” (BEST PATHS) under Grant 612748. The authors would like to thank Prof. Thorsten Stoesser, Director of the Hydro-environmental Research Centre of the School of Engineering, Cardiff University, for his support in this work.

## 9. References

- [1] Khan, M. J., Bhuyan, G., Iqbal, M. T., Quiacoe, J. E.: 'Hydrokinetic energy conversion systems and assessment of horizontal and vertical axis turbines for river and tidal applications: A technology status review', *Applied Energy*, 2009, 86, (10), pp. 1823–1835
- [2] Khan, M. J., Iqbal, M. T., Quiacoe, J. E.: 'Effects of Efficiency Nonlinearity on the Overall Power Extraction: A Case Study of Hydrokinetic-Energy-Conversion Systems', *IEEE Transactions on Energy Conversion*, 2011, 26, (3), pp. 911–922
- [3] Hauck, M., Rumeau, A., Bratcu, A. I., Bacha, S., Munteanu, I., Roye, D.: 'Identification and control of a river-current-turbine generator — application to a full-scale prototype', *IEEE Transactions on Sustainable Energy*, 2018, 9, (3), pp. 1365–1374
- [4] Khan, M. J., Iqbal, M. T., Quiacoe, J. E.: 'River current energy conversion systems: Progress, prospects and challenges', *Renewable and Sustainable Energy Reviews*, 2008, 12, (8), pp. 2177–2193
- [5] Anaya-Lara, O., Jenkins, N., Ekanayake, J., Cartwright, P., Hughes, M.: 'Wind energy generation: Modelling and control' (Wiley, UK, 2009)
- [6] Chowdhury, M. M., Haque, M. E., Saha, S., Mahmud, M. A., Gargoom, A., Oo, A. M. T.: 'An Enhanced Control Scheme for an IPM Synchronous Generator Based Wind Turbine With MTPA Trajectory and Maximum Power Extraction', *IEEE Transactions on Energy Conversion*, 2018, 33, (2), pp. 556–566

- [7] Whitby, B., Ugalde-Loo, C. E.: 'Performance of Pitch and Stall Regulated Tidal Stream Turbines', *IEEE Transactions on Sustainable Energy*, 2014, 5, (1), pp. 64–72
- [8] Mirecki, A., Roboam, X., Richardeau, F.: 'Architecture Complexity and Energy Efficiency of Small Wind Turbines', *IEEE Transactions on Industrial Electronics*, 2007, 54, (1), pp. 660–670
- [9] Bhende, C. N., Mishra, S., Malla, S. G.: 'Permanent Magnet Synchronous Generator-Based Standalone Wind Energy Supply System', *IEEE Transactions on Sustainable Energy*, 2011, 2, (4), pp. 361–373
- [10] Koutroulis, E., Kalaitzakis, K.: 'Design of a maximum power tracking system for wind-energy-conversion applications', *IEEE Transactions on Industrial Electronics*, 2006, 53, (2), pp. 486–494
- [11] Putri, R.I., Pujiantara, M., Priyadi, A., Ise, T., Purnomo, M.H.: 'Maximum power extraction improvement using sensorless controller based on adaptive perturb and observe algorithm for PMSG wind turbine application', *IET Electric Power Applications*, 2018, 12, (4), pp. 455–462
- [12] Daili, Y., Gaubert, G.-P., Rahmani, L.: 'New control strategy for fast-efficient maximum power point tracking without mechanical sensors applied to small wind energy conversion system', *Journal of Renewable and Sustainable Energy*, 2015, 7, (4), pp. 43102
- [13] Hui, J. C. Y., Bakhshai, A., Jain, P. K.: 'A Sensorless Adaptive Maximum Power Point Extraction Method With Voltage Feedback Control for Small Wind Turbines in Off-Grid Applications', *IEEE Journal of Emerging and Selected Topics in Power Electronics*, 2015, 3, (3), pp. 817–828
- [14] Kazmi, S. M. R., Goto, H., Guo, H. J., Ichinokura, O.: 'A Novel Algorithm for Fast and Efficient Speed-Sensorless Maximum Power Point Tracking in Wind Energy Conversion Systems', *IEEE Transactions on Industrial Electronics*, 2011, 58, (1), pp. 29–36
- [15] Hussain, J., Mishra, M. K.: 'Adaptive Maximum Power Point Tracking Control Algorithm for Wind Energy Conversion Systems', *IEEE Transactions on Energy Conversion*, 2016, 31, (2), pp. 697–705
- [16] Mohamed, A. Z., Eskander, M. N., Ghali, F. A.: 'Fuzzy logic control based maximum power tracking of a wind energy system', *Renewable Energy*, 2001, 23, (2), pp. 235–245
- [17] Elnaggar, M., Saad, M. S., Fattah, H. A. A., Elshafei, A.L.: 'L<sub>1</sub> adaptive fuzzy control of wind energy conversion systems via variable structure adaptation for all wind speed regions', *IET Renewable Power Generation*, 2017, 12, (1), pp. 18–27
- [18] Alvarez, A., Rico-Secades, M., Corominas, E. L., Huerta-Medina, N., Soler Guitart, J.: 'Design and control strategies for a modular hydrokinetic smart grid', *International Journal of Electrical Power & Energy Systems*, 2018, 95, pp. 137–145
- [19] Moreno Vásquez, F. A., De Oliveira, T. F., Brasil Junior, A. C. P.: 'On the electromechanical behavior of hydrokinetic turbines', *Energy Conversion and Management*, 2016, 115, pp. 60–70
- [20] Zhang, J., Leontidis, V., Dazin, A., Tounzi, A., Delarue, P., Caignaert, G., Piriou, F., Libaux, A.: 'Canal lock variable speed hydropower turbine design and control', *IET Renewable Power Generation*, 2018, 12, (14), pp. 1698–1707
- [21] Ashourianjozdani, M. H., Lopes, L. A. C., Pillay, P.: 'Power control strategy for fixed-pitch PMSG-based hydrokinetic turbine', *Proc. 2016 IEEE International Conference on Power Electronics, Drives and Energy Systems (PEDES)*, Trivandrum, India, December 2016, pp. 1–6.
- [22] Cavagnaro, R. J., Polagye, B., Thomson, J., Fabien, B., Forbush, D., Kilcher, L., Donegan, J., McEntee, J.: 'Emulation of a Hydrokinetic Turbine to Assess Control and Grid Integration', *Proc. 11th European Wave and Tidal Energy Conference (EWTEC)*, Nantes, France, September 2015, pp. 10A3-4-2–10A3-4-8
- [23] Guo, B., Mohamed, A., Bacha, S., Alamir, M.: 'Variable speed micro-hydro power plant: Modelling, losses analysis, and experiment validation', *Proc. 2018 IEEE International Conference on Industrial Technology (ICIT)*, Lyon, France, April 2018, pp. 1079–1084
- [24] Borkowski, D.: 'Maximum Efficiency Point Tracking (MEPT) for Variable Speed Small Hydropower Plant with Neural Network Based Estimation of Turbine Discharge', *IEEE Transactions on Energy Conversion*, 2017, 32, (3), pp. 1090–1098
- [25] Khan, M. J., Iqbal, M. T., Quiacoe, J. E.: 'A Technology Review and Simulation Based Performance Analysis of River Current Turbine Systems'. *Proc. 2006 Canadian Conference on Electrical and Computer Engineering*, Ottawa, Canada, May 2006, pp. 2288–2293
- [26] Licari, J., Ugalde-Loo, C. E., Liang, J., Ekanayake, J., Jenkins, N.: 'Torsional Damping Considering both Shaft and Blade Flexibilities', *Wind Engineering*, 2012, 36, (2), pp. 181–196
- [27] Licari, J., Ugalde-Loo, C. E., Ekanayake, J., Jenkins, N.: 'Damping of Torsional Vibrations in a Variable-Speed Wind Turbine', *IEEE Transactions on Energy Conversion*, 2013, 28, (1), pp. 172–180
- [28] Krishnan, R.: 'Permanent Magnet Synchronous and Brushless DC Motor Drives' (Taylor & Francis, USA, 2010)
- [29] Melfi, M. J., Evon, S., McElveen, R.: 'Induction versus permanent magnet motors', *IEEE Industry Applications Magazine*, 2009, 15, (6), pp. 28–35
- [30] Mohan, N., Undeland, T., Robbins, W.: 'Power Electronics-Converters, Applications and Design' (Wiley, USA, 1989)
- [31] LabJack Corporation, 'USB Multifunction DAQ', <https://labjack.com/products/u6>, accessed 20<sup>th</sup> July 2018

- [32] Harries, T., Kwan, A., Brammer, J., Falconer, R.: 'Physical testing of performance characteristics of a novel drag-driven vertical axis tidal stream turbine with comparisons to a conventional Savonius', *International Journal of Marine Energy*, 2016, 14, pp. 215–228
- [33] Betz, A.: 'Windenergie und ihre ausnutzung durch windmühlen' (Vandenhoeck, Germany, 1926)
- [34] Runge, S., Stoesser, T., Morris, E., White, M.: 'Technology Readiness of a Vertical-Axis Hydro-Kinetic Turbine', *Journal of Power and Energy Engineering*, 2018, 6, (8), pp. 63–85
- [35] Knight, A. M., Peters, G. E.: 'Simple wind energy controller for an expanded operating range', *IEEE Transactions on Energy Conversion*, 2005, 20, (2), pp. 459–466
- [36] Rossander, M., Goude, A., Eriksson, S.: 'Mechanical Torque Ripple From a Passive Diode Rectifier In a 12 kW Vertical Axis Wind Turbine', *IEEE Transactions on Energy Conversion*, 2017, 32, (1), pp. 164–171.
- [37] Michas, M., Ugalde-Loo, C. E., Jenkins, N.: 'Grid code compliance and ancillary services provision from DFIG and FRC-based wind turbines'. Proc. 2016 51<sup>st</sup> International Universities' Power Engineering Conference (UPEC), Coimbra, Portugal, September 2016, pp. 1–6

## 10. Appendix

### 10.1. *Estimation of the system inertia*

For the estimation of the inertia of each turbine, the mass of each blade,  $M_{1b}$ , is calculated using  $M_{1b} = V_{blade} \cdot d_{blade}$ , where  $V_{blade}$  is the volume and  $d_{blade}$  is the density of each blade. Assuming the blade is a point mass rotating in a distance  $R$  from the rotor of the vertical-axis turbine, the inertia of each blade is calculated using  $J_{1b} = M_{1b} \cdot R^2$ , where  $R$  is the radius of each turbine. Each turbine consists of three blades and, thus, the inertia of each turbine is given by  $J_{1t} = 3J_{1b}$ . The total inertia of the two turbines, referring to the low speed shaft, is calculated using  $J_{2t} = 2J_{1t}$ . Therefore, the inertia of the two turbines referring to the common shaft is given by  $J_{2t, csh} = \frac{J_{2t}}{N^2}$ .